ELSEVIER

Contents lists available at ScienceDirect

Additive Manufacturing

journal homepage: www.elsevier.com/locate/addma





Ultrafine-grained Fe-TiB₂ high-modulus nanocomposite steel with high strength and isotropic mechanical properties by laser powder bed fusion

Shuai Feng ^{a,b}, Shuai Guan ^{a,*}, Shengbiao Zhang ^a, Shahryar Mooraj ^a, Matthew Luebbe ^c, Xuesong Fan ^d, Kevin A. Beyer ^e, Tianyi Li ^e, Jian Liu ^a, Jian Kong ^b, Peter K. Liaw ^d, Haiming Wen ^c, Simos Gerasimidis ^{f,*}, Wen Chen ^{a,*}

- ^a Department of Mechanical and Industrial Engineering, University of Massachusetts, Amherst, MA 01003, USA
- ^b School of Materials Science and Engineering, Nanjing University of Science and Technology, 200 Xiaolingwei, Nanjing 210094, PR China
- ^c Department of Materials Science and Engineering, Missouri University of Science and Technology, Rolla, MO 65409, USA
- ^d Department of Materials Science and Engineering, The University of Tennessee, Knoxville, TN 37996, USA
- ^e X-ray Science Division, Argonne National Laboratory, Lemont, IL 60439, USA
- f Department of Civil and Environmental Engineering, University of Massachusetts, Amherst, MA 01003, USA

ARTICLEINFO

Keywords: Additive manufacturing High-modulus steel In situ alloying Metal matrix composite Mechanical properties

ABSTRACT

Fe-TiB2 metal matrix composite, also called high-modulus steels (HMSs), are of great interest for applications in fuel-efficient transportation infrastructure, aerospace, and wear industries due to their high specific stiffness and yield strength. However, conventional cast Fe-TiB2 HMSs often contain coarse and sharp-edged TiB2 particles which easily trigger premature cracking during loading. Here, we synthesized a Fe-TiB2 nanocomposite HMS via laser powder bed fusion (LPBF) additive manufacturing of mixed micro-sized powders of Fe, Ti, and Fe₂B. We investigated the microstructure formation and mechanical behavior of the Fe-TiB2 HMS. We found that in situ chemical reaction of Ti and Fe₂B enables the formation of TiB₂ particles at nanoscale during rapid solidification of LPBF. These nanoscale TiB2 particles can serve as heterogeneous nucleation sites and promote the formation of ultrafine and equiaxed α -Fe grains with random crystallographic textures, which differ from many other additively manufactured (AM) metal alloys characteristic of strong crystallographic textures. As such, isotropic mechanical properties were achieved in the AM Fe-TiB $_2$ nanocomposite HMS with a high elastic modulus of \sim 240 GPa, an exceptional yield strength of \sim 1450 MPa, and a large plasticity of \sim 20% under compression. Quantitative analysis reveals that the high yield strength primarily originates from strengthening contributions of the ultrafine grains with an average grain size of ~450 nm, the nanoscale TiB2 reinforcing particles of 20-180 nm, and a high density of printing-induced dislocations of the order of 10¹⁵ m⁻². In situ synchrotron high-energy X-ray diffraction unveils the load partitioning from the softer α -Fe matrix to the stiffer and stronger TiB₂ nanoparticles, contributing to the sustained strain hardening during compression. Our work not only provides a general pathway for achieving high-performance metal matrix nanocomposites by in situ chemical reaction and precipitation of ceramic nanoparticles during additive manufacturing, but also offers mechanistic insights into the deformation mechanism of nanoparticle-reinforced HMS composites.

1. Introduction

High-modulus steels (HMSs) are workhorse materials for fuelefficient transportation infrastructure, aerospace and wear industries owing to their high specific stiffness and yield strength [1,2]. The HMSs community has so far strongly focused on ceramic particles-reinforced Fe-based metal matrix composites, where light, stiff, and strong ceramic particles contribute to a significant increase in both specific stiffness and specific yield strength [3,4]. Among various ceramic phases, TiB₂ ceramic particles have received the most attention [5–7]. In addition to their excellent physical and mechanical properties, e.g., a low density of 4.52 g/cm³ and a high Young's modulus of 565 GPa, TiB₂ ceramic particles are thermodynamically stable and can be in situ synthesized in the Fe-Ti-B steel composite system [2,8–10]. Additionally,

E-mail addresses: shuaiguan@umass.edu (S. Guan), sgerasimidis@umass.edu (S. Gerasimidis), wenchen@umass.edu (W. Chen).

^{*} Corresponding authors.

TiB₂ reinforcement exhibits favorable wettability and metallurgical bonding with the α -Fe matrix [11–13]. So far, many attempts have been made towards high performance Fe-TiB2 HMSs by casting. For example, Huang et al. reported that a cast Fe-based HMS reinforced with 14 volume percent (vol%) TiB2 particles exhibited a low density of 7.14 g/cm³ and a high Young's modulus of 253 GPa [14]. Similarly, Li et al. also casted an Fe-based HMS reinforced with 15 vol% TiB2 particles, presenting a specific stiffness of 34 GPa·cm³·g⁻¹, a specific yield strength of 104 MPa·cm³·g⁻¹, and a specific ultimate tensile strength of 130 MPa·cm³·g⁻¹ [15]. These attractive properties make Fe-TiB₂ HMSs well outperform conventional monolithic steels. However, the TiB2 particles formed during conventional casting are often sharp-edged and tend to coarsen owing to insufficient cooling rates. Sharp-edged and coarse particles not only weaken the interfacial decohesion [12,16], but also easily generate substantial local stress concentration and lead to early crack initiation [17-19]. To control the morphology and size of TiB₂ particles, Springer et al. used levitation melting coupled with splat cooling to process Fe-TiB₂ HMSs, and the intrinsically high cooling rates facilitate the in situ formation of spherical TiB2 particles down to nanoscale sizes [20]. However, such processing routes are not readily applicable for fabricating bulk HMS parts.

Through the past two decades, laser powder bed fusion (LPBF) additive manufacturing is developing rapidly due to its unique capability of printing net-shaped parts directly from a computer-aided design model [21-28]. This emerging technique enables the design freedom for complex geometry and requires little or no post tooling. Additionally, LPBF is featured by localized solidification in the melt pool with a high cooling rate up to $\sim 10^6$ K/s, resulting in highly refined and heterogeneous microstructures that give rise to unusual mechanical properties not readily achievable by conventional processing routes [29,30]. Driven by these promising outcomes, LPBF has also been employed to process HMSs in recent years [31]. For example, Springer et al. successfully fabricated Fe-TiB2 HMS by LPBF processing of Fe-Ti-B pre-alloyed powders [31]. Their study shows that the rapid solidification during LPBF leads to the formation of TiB2 nanoparticles homogenously dispersed in the α -Fe matrix. However, numerous metallurgical defects such as pores and cracks were frequently observed that prevented a thorough evaluation of the macroscopic mechanical properties of the additively manufactured (AM) Fe-TiB2 HMS. In addition, the preparation of customized Fe-Ti-B pre-alloyed powder feedstocks is time-consuming and costly. To address this challenge, a cost-effective alternative is of significant interest by directly employing mixtures of multiple commercially available powders for the LPBF process. Although the direct incorporation of TiB₂ particles has been successfully employed for AM metal alloys (e.g., steel and Al alloys) to produce a fine-grained microstructure with a random crystallographic orientation by LPBF [32,33], these ex-situ metal-matrix composites face challenges such as poor wetting at the matrix/ceramic particle interface and inhomogeneous dispersion of ceramic particles in the matrix [34,35]. Compared with the ex-situ routes, the in-situ process has significant superiorities such as uniform distribution of reinforcements, finer reinforcement sizes, and thermodynamically stable reinforcement in the metal matrix composites [36].

In the present work, we fabricated in-situ Fe-TiB $_2$ nanocomposite HMS by LPBF of mixed powders of Fe, Ti, and Fe $_2$ B, which are all commercially available. LPBF of in-situ Fe-TiB $_2$ nanocomposite HMS involves chemical reaction of primary powders, enabling in-situ formed and uniformly distributed TiB $_2$ nanoparticles in the matrix. The LPBF HMS exhibits excellent mechanical properties with a high elastic modulus of ~ 240 GPa, an ultrahigh yield strength of ~ 1450 MPa, and a large compressive plasticity of $\sim 20\%$. In addition, unlike many other AM metal alloys that demonstrate a strong mechanical anisotropy, the LPBF HMS possesses isotropic mechanical properties due to the random crystallographic texture. Our work provides a general pathway for achieving high performance metal matrix nanocomposites by in situ chemical reaction and precipitation of ceramic nanoparticles during

laser additive manufacturing.

2. Experimental details

2.1. Powder characteristics

A target powder composition of Fe-6.4Ti-2.6B (wt%) were prepared for LPBF from mixed micro-sized powders of Fe, Ti, and Fe₂B that are commercially available. Here the target composition corresponds to the near-eutectic composition of ~ 13.65 vol% TiB₂ in the Fe-Ti-B system, leading to a desirably low melting temperature of \sim 1400 $^{\circ}\text{C}$ [20] and minimal solidification interval [37], which are beneficial for avoiding hot cracking during AM process. Commercially available high purity elemental Fe (99.99 wt%), Ti (99.99 wt%), and Fe₂B (99.9 wt%) powders were purchased from Atlantic Equipment Engineers, Inc. USA. The Fe and Ti elemental powders are spherical with a size range of $5-53 \mu m$ and 5-38 µm, respectively, while the Fe₂B powders are irregular with a size of 1–25 μm (Fig. 1a-d). The mass median diameters of the Fe, Ti and Fe₂B powders are 31.2, 19.6, and 8.6 µm, respectively. Note that Fe₂B instead of B was used due to its much lower melting point that facilitates in situ alloving during rapid solidification. These constituent powders were mixed by a low-energy T2F Turbula Heavy-Duty Shaker-Mixer for 2 h. A typical scanning electron microscopy (SEM) image and corresponding elemental maps using energy-dispersive x-ray spectroscopy (EDS) in Fig. 1e show that the constituent powders were homogeneously mixed.

2.2. LPBF process optimization

The mixed powders were loaded into an M290 LPBF system (EOS GmbH, Munich, Germany), which is equipped with a 400 W Yb-fiber laser of a spot size of $100~\mu m$. We first performed a standard single-track study to narrow down the process window, encompassing 70 different combinations of laser powers and laser scan speeds, as summarized in Table S1 in Supplementary Information. The geometric characteristics of these single tracks were analyzed by the optical microscopy (OM, BX53M, Olympus, Tokyo, Japan). Specifically, these single-track deposits were sectioned, polished, and chemically etched, using a 5% nitric acid solution by volume. The melt pool depth was determined by measuring the distance from the substrate surface to the melt pool bottom. The melt pool width was extracted by measuring the distance across the two intersection points between the single track and substrate surface.

Based on the narrowed process window determined from singletrack experiments, a series of cubic samples of $8 \times 8 \times 8 \text{ mm}^3$ were fabricated with 16 different parameters (see Table S2 in Supplementary Information). The layer thickness and hatch distance of those cubic samples were kept constant at 40 µm and 80 µm, respectively, based on empirical relationships and our previous work [29,38-40]. To reduce the potential crystallographic anisotropy [41], a bi-directional scan mode with 90° rotation between successive layers were adopted for these bulk samples. The density of these bulk samples was determined by an AccuPyc II 1340 gas pycnometer (Micromeritics, Norcross, GA, USA). The metallurgical defects of these bulk samples were investigated by OM. Based on the density and defect levels of these bulk samples, the optimal process parameters were determined: a laser power of 300 W, a laser scan speed of 500 mm/s, a layer thickness of 40 µm, and a hatching distance of 80 µm. The bulk samples built with these process parameters were used for subsequent microstructural and mechanical characterizations.

2.3. Microstructural and mechanical characterizations

The LPBF HMS samples were sectioned perpendicular (top view) and parallel (side view) to the building direction, respectively, then progressively ground with SiC grinding papers for metallographic

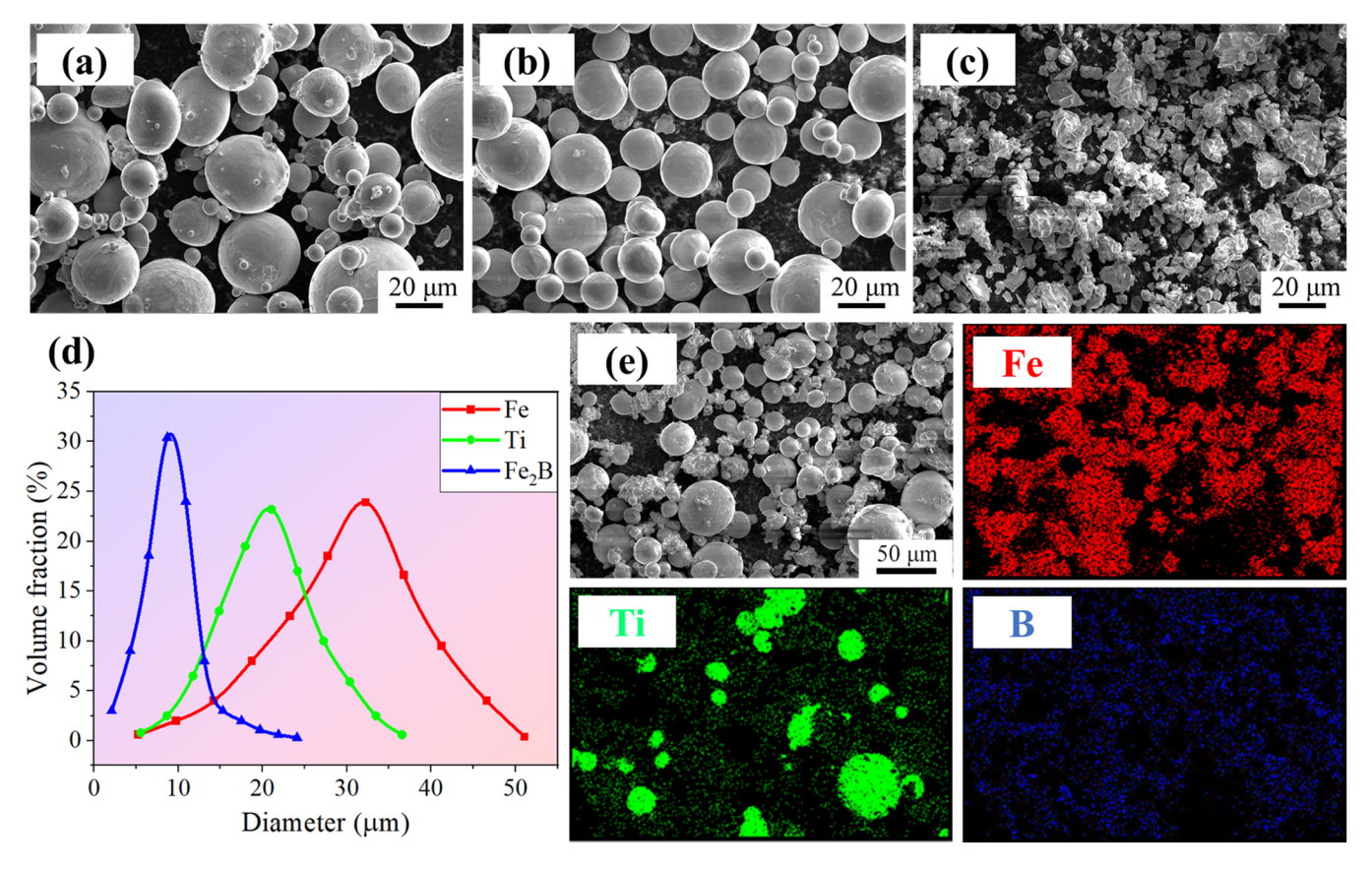


Fig. 1. SEM images showing the characteristic morphology of (a) Fe, (b) Ti, (c) Fe₂B powders, and (d) corresponding powder size distributions. (e) A typical SEM image presenting the Fe/Ti/Fe₂B mixtures and the elemental maps.

examination.

A field-emission scanning electron microscopy (SEM, Leo Gemini 1525, Oberkochen, Germany) was applied to characterize the microstructure. The SEM images were collected in the scanning electron microscope at three different magnifications: $200 \times (a pixel size of$ 0.15 μ m), 1500 \times (a pixel size of 0.025 μ m), and 30,000 \times (a pixel size of 1.8 nm). The TiB2 volume fraction was estimated from SEM images using the public-domain software ImageJ [42,43]. More than 20 SEM images were taken, with each SEM image covering an area of $3.8 \times 3.8 \ \mu m^2$. To get physical insight into the formation of TiB₂ phase, Scheil-Gulliver non-equilibrium solidification calculation was performed with Thermo-Calc software (v. 2020b) with a steel/Fe thermodynamic database (TCFE10 v. 10.1). Specimens for electron backscatter diffraction (EBSD) imaging were further mechanically grinded using 20 nm oxide polishing suspension, followed by vibratory polishing to remove the surface deformation layer induced by mechanical polishing. EBSD characterization was performed using a field emission SEM (Carl Zeiss Auriga 45-66, Jena, Germany) equipped with an Oxford Instruments Aztec 2.0 EBSD system (Channel 5 software). The step size for the EBSD scan was 40 nm. Transmission electron microscopy (TEM) samples were lifted out from the polished samples, and then thinned down to below 100 nm using focused ion beam (FIB) on a Thermo Scientific Scios Dual-Beam (Thermo Fisher Scientific, USA). TEM characterization was performed utilizing a FEI Tecnai F20 (FEI Company, USA).

An Instron 5969 testing machine (Instron, USA) was employed for uniaxial compression tests with a strain rate of $5\times 10^{-4}~\text{s}^{-1}$. A noncontact AVE2 video extensometer was employed during compression tests to precisely measure the strain. For compression tests, following the general ASTM E9–09 standard, an aspect ratio of 2 was adopted. Compression pillars with dimensions of 2 mm \times 2 mm \times 4 mm were cut along both top- and side-view planes to study the orientation effect.

Three tests were performed for each orientation. Vickers hardness tests were performed via a Vickers microhardness tester (ALPHA HMT-2000Z) with a load of 500 g and a dwell time of 15 s

2.4. In-situ synchrotron-based high-energy X-ray diffraction (HE-XRD)

The deformation micro-mechanisms of our LPBF HMS were studied using in-situ compression experiments under HE-XRD at the beamline 11-ID-C at the Advanced Photon Source, Argonne National Laboratory. A 0.5×0.5 mm² X-ray beam size was used, with a wavelength $\lambda = 0.1173$ Å and a corresponding energy of 105.7 keV. We used the LaB₆ standard material to calibrate the distance between the detector and the sample. We collected two-dimensional (2D) XRD patterns and then processed the data by GSAS II software [44]. One-dimensional (1D) XRD patterns were obtained by the integration of the 2D patterns along a specific azimuth angle over a range of \pm 5°. The interplanar spacing (*d*-spacing) of each (*hkl*) crystalline plane was converted from the diffraction angle, θ , based on the Bragg's equation ($2 \sin \theta = \lambda$). Then the lattice strain, ε_{hkl} , of each (*hkl*) crystalline plane can be calculated from $\varepsilon_{hkl} = (d_{hkl} - d_{hkl,0})/d_{hkl,0}$, where $d_{hkl,0}$ and d_{hkl} are the interplanar spacings without and with an applied stress, respectively.

3. Results and discussion

3.1. Densification

3.1.1. Single-track samples

A preliminary printability diagram (Fig. 2a) was established, based on experimental observations of the geometric characteristics of 70 single-track deposits obtained with different laser powers and laser scan speeds. Four distinct regions can be distinguished from the printability diagram in Fig. 2a, with representative geometric characteristics shown

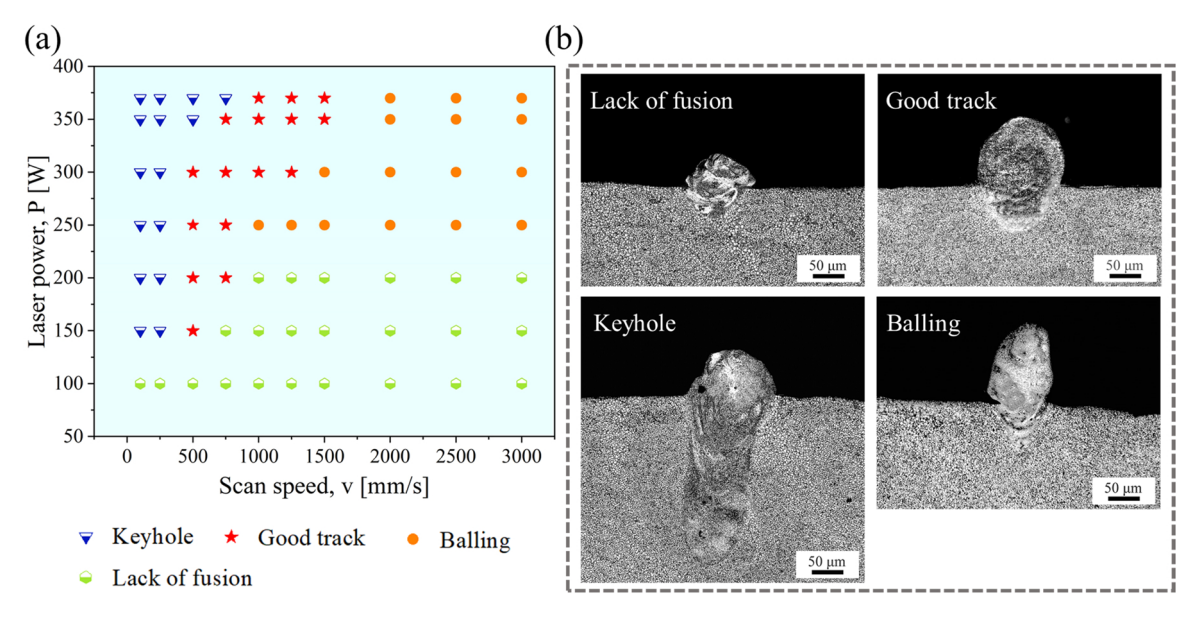


Fig. 2. (a) A preliminary printability diagram established based on the experimental observations of 70 single-track deposits obtained with a wide laser power - laser scan speed region. Keyhole, good track, balling, and lack of fusion are marked with different symbols and colors. (b) Representative melt pool cross sections showing the lack of fusion, good track, keyhole, and balling, respectively.

in Fig. 2b. First, lack-of-fusion defects tend to appear at low laser powers and high laser scan speeds, which can be attributed to the low energy input and thus the insufficient penetration into the substrate [45,46]. Second, keyholing prevails at low laser scan speeds and high laser powers. It is generally believed that keyholing occurs owing to the over-high energy input, and as a direct result, the liquid metal may evaporate and induce vapor cavities [47,48]. Moreover, vapor cavities are sometimes enclosed before gas can escape. Hence, the gas is trapped and retained inside the deposit, becoming unwanted pores. Third, at high laser powers (> 200 W) and very high laser scan speeds (1000 -3000 mm/s), a balling phenomenon was observed. In this case, the melt pool tends to break into discontinuous droplets due to the Plateau-Rayleigh capillary instability [49]. Such balling effect often results in the void formation, poor surface roughness, and even delamination, all of which deteriorate the mechanical properties of the deposited parts. Besides these three types of defects, we also observed that good single-track deposits (asterisk symbols in Fig. 2a) can be obtained with 16 combinations of laser powers and laser scan speeds, as listed in Table S1.

3.1.2. Bulk samples

Based on the results of single-track experiments, bulk samples of $8 \times 8 \times 8 \text{ mm}^3$ were fabricated using 16 different parameter combinations (see Table S2). The density analysis results are shown in Fig. 3, accompanied by several typical optical micrographs showing different types of metallurgical defects. At low volumetric energy density (VED) values (e.g., 83.3 J/mm³), the relative density is low, and this is due to the formation of lack-of-fusion pores. The increase of the VED (e.g., 109.37 J/mm³, and 156.25 J/mm³) progressively leads to a better densification with fewer micropores and gradually improved sphericity. The VED of 187.5 J/mm³ leads to the highest relative density of 99.32 \pm 0.33% and the corresponding porosity is 0.68 \pm 0.33%, with a Gaussian-type pore size distribution ranging from 0.2 to 15 µm (see Fig. S1 in the Supplementary Information). It should be noted that the irregular shape of the microscale Fe₂B powders (Fig. 1c) in the feedstock powders may be detrimental to the powder flowability and packing density. However, this issue can be mitigated by the high VED value of 187.5 J/mm³ which facilitates enhanced Marangoni flow and hence improved gas escape and elemental homogeneity [50,51]. As a result, a relative density as high as $99.32 \pm 0.33\%$ was achieved. It is worth

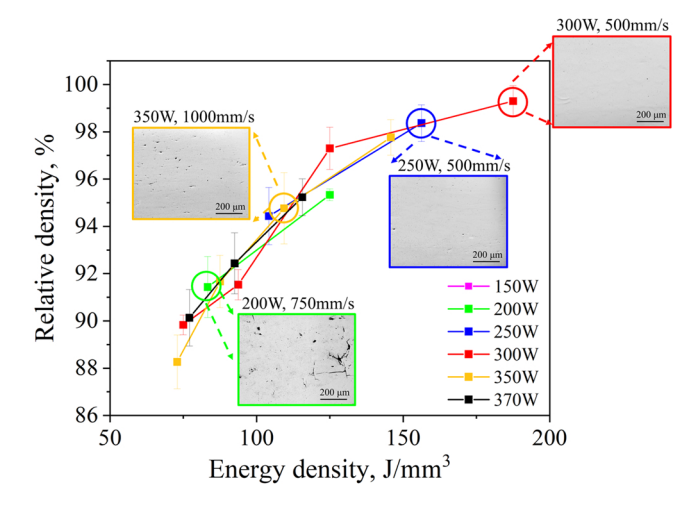


Fig. 3. Relatively density of the LPBF HMS bulk samples manufactured at various laser energy densities. The density measurements were carried out using a He gas pycnometer.

mentioning that $Fe-TiB_2$ composites have superior wear resistance [52] and those samples in sub-optimal processing conditions (higher porosity) have potential applications in the field of grinding wheel [53–55].

3.2. Phases and microstructures

3.2.1. Fe-Ti B_2 dual-phase structure

Fig. 4 shows the 1D HE-XRD profile of LPBF HMS in the as-printed state, which was integrated over the entire 360° . The HE-XRD pattern demonstrates a dual-phase structure in the LPBF HMS, i.e., the α -Fe phase with a body-centered-cubic (BCC) structure and the TiB₂ phase with a hexagonal-close-packed (HCP) structure. The TiB₂ peaks can be clearly observed in the enlarged diffraction pattern, as shown in Fig. 4b. Based on a quantitative Rietveld refinement analysis, the lattice parameter of $a_1 = 2.87023$ Å for α -Fe phase, whereas the calculated lattice parameters for the TiB₂ phase are $a_2 = 3.03043$ Å and c = 3.21606 Å. Moreover, the refined phase fraction of the TiB₂ phase is

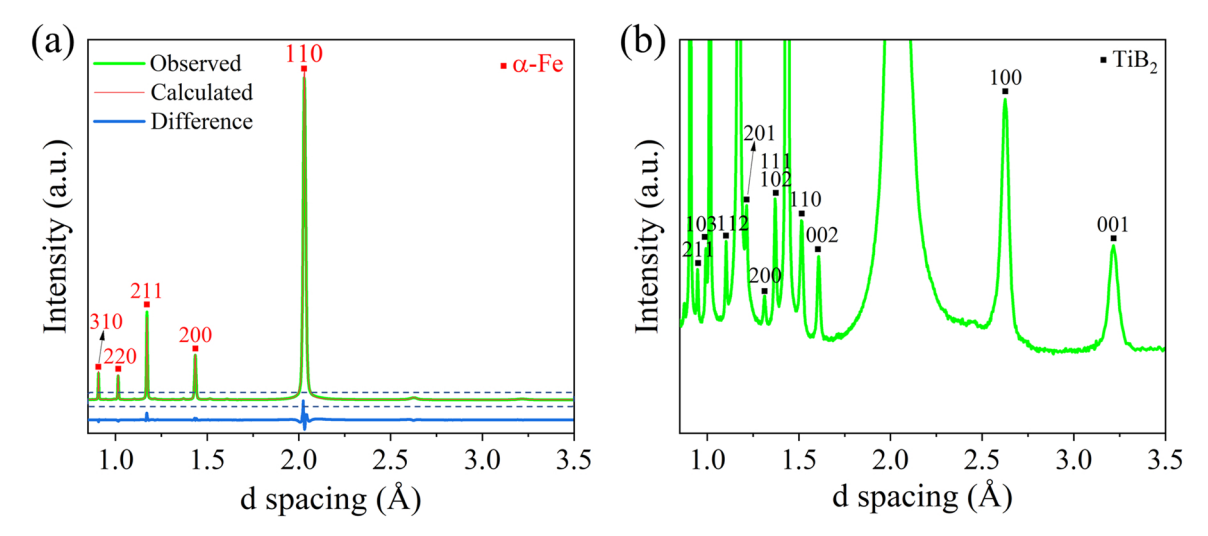


Fig. 4. (a) 1D HE-XRD profile integrated over the entire 360° of LPBF HMS in the as-printed state. (b) Enlarged diffraction pattern of the rectangular region in (a) showing the TiB_2 diffraction peaks.

estimated to be \sim 13.2%.

As presented in Fig. 5a, the LPBF HMS exhibits typical "fish-scale" melt pools, which are common for AM materials [29,30]. Consistent with the HE-XRD measurements, a dual-phase microstructure with an α -Fe phase in bright contrast and TiB₂ phase in black contrast was observed (Fig. 5b-d). Contrary to common AM metal alloys that are often composed of columnar grains [21,56,57], the α -Fe grains are highly equiaxed. The TiB₂ particles of 20–180 nm in diameter are dispersed in the α -Fe matrix, preferentially at the grain boundaries. Interestingly, both the α -Fe grains and the TiB₂ nanoparticles in the heat-affected zone (HAZ) are slightly coarser than those in the melt pool interior (Fig. 5b-d). This feature may result from the in situ thermal-cycling-induced grain-coarsening effect in the HAZ during laser scanning of successive tracks or layers [58]. In addition, EDS mapping

was performed over a region containing a melt pool boundary, and no obvious chemical differences were detected across the melt pool boundary, as shown in Fig. S2 in the Supplementary Information. Thus, a change in contrast between the top and bottom of single layers in Fig. 5a is presumably attributed to the differences in grain sizes. Based on these SEM micrographs, the volume fraction of the TiB₂ nanoparticles is estimated to be $\sim 13\%$, which is coincident with the Rietveld refinement analysis of the 1D HE-XRD pattern.

We further performed TEM experiments to determine the phase constitutes of the LPBF HMS specimen. The TiB_2 nanoparticles contrast well under TEM, appearing as small black dots in Fig. 6a. Several but not all of the grains are visible under TEM with an objective aperture contrast. To confirm that the particles are TiB_2 , a scanning transmission electron microscopy (STEM) image with EDS mapping was collected,

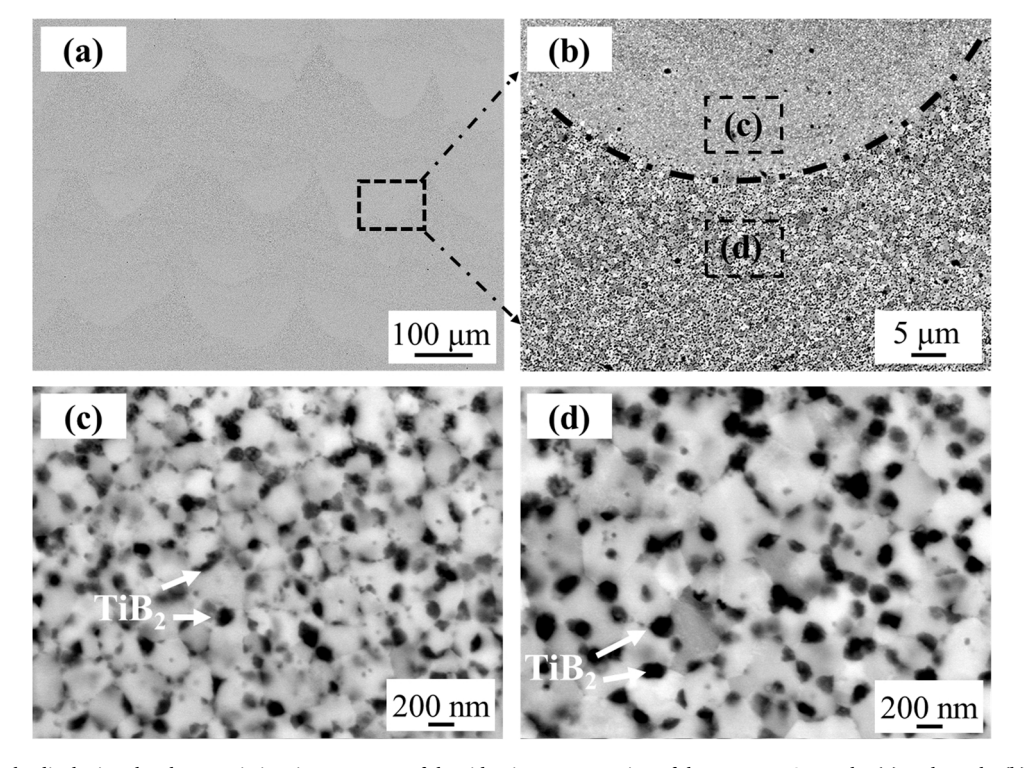


Fig. 5. SEM micrographs displaying the characteristic microstructure of the side-view cross-section of the LPBF HMS sample. (a) Melt pools. (b) A melt pool contains finer grains in the melt pool interior and relatively coarser grains in the HAZ below the melt pool boundary. (c) Finer grains. (d) Coarser grains.

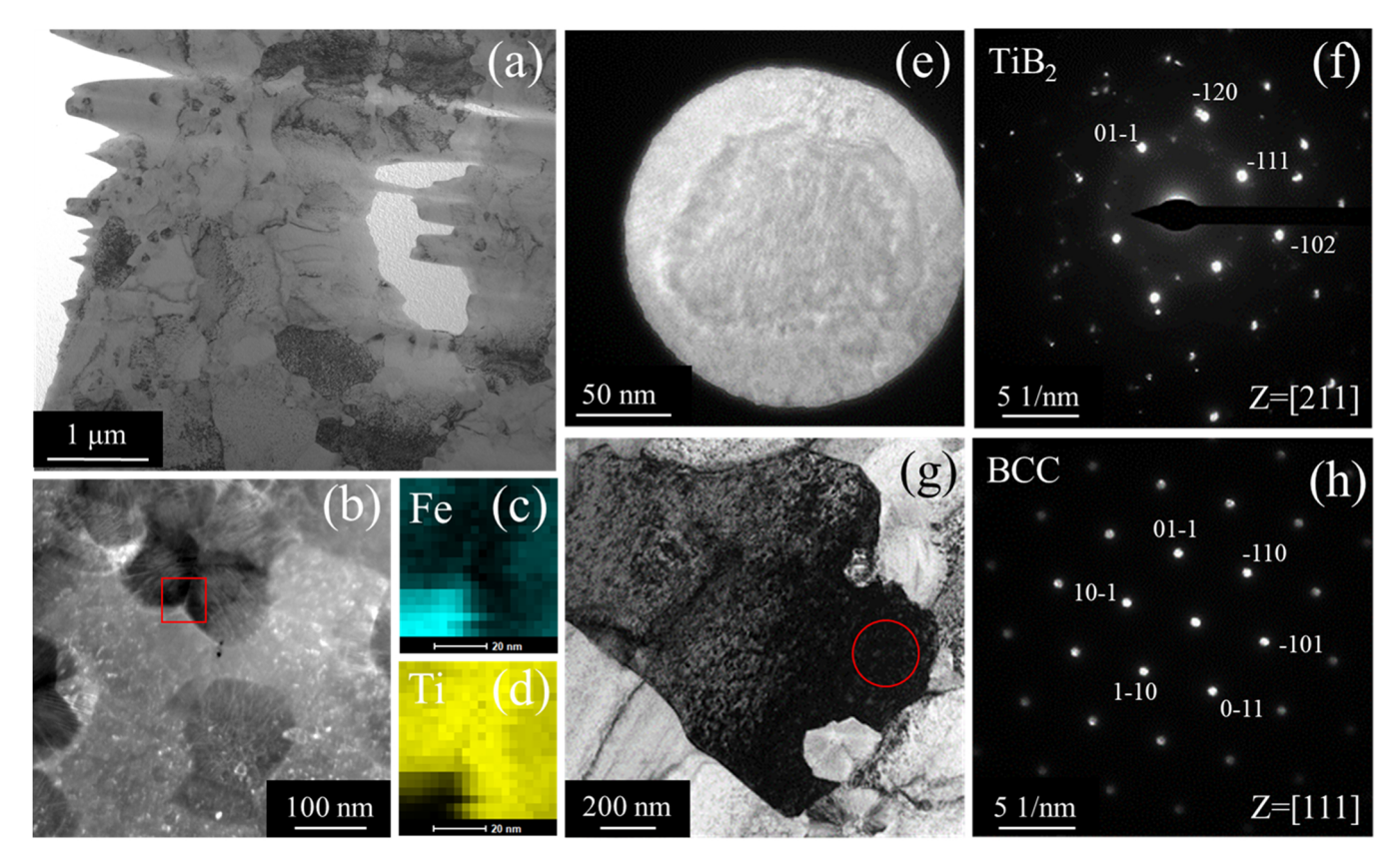


Fig. 6. TEM characterization of LPBF HMS. (a) A representative TEM image of α -Fe grains and TiB₂ nanoparticles. (b) A STEM image of TiB₂ nanoparticles, with (c) Fe and (d) Ti STEM-EDS maps of the highlighted region in (b). (e) TiB₂ nanoparticle in the selected area aperture, along with (f) the SAED pattern of the particle in (e). (g) The α -Fe grain along with (h) the SAED pattern of the highlighted region in (g).

showing the Ti enrichment in the particles (Fig. 6b-d). Confirmation of the crystal structure of both HCP TiB₂ nanoparticles and BCC α -Fe phase were also performed, using selected area electron diffraction (SAED), shown in Fig. 6e-h.

The above HE-XRD, SEM, and TEM characterizations concurrently reveal an Fe-TiB₂ dual-phase structure. It naturally follows to analyze the phase formation. For the complex Fe-Ti-Fe₂B system, several chemical reactions may occur and are listed as follows [59–63]:

$$Fe + Ti = FeTi (1)$$

$$2Fe + Ti = Fe_2Ti (2)$$

$$Ti + 2B = TiB_2 (3)$$

$$Ti + B = TiB (4)$$

$$Fe + B = FeB (5)$$

$$2Fe + B = Fe2B (6)$$

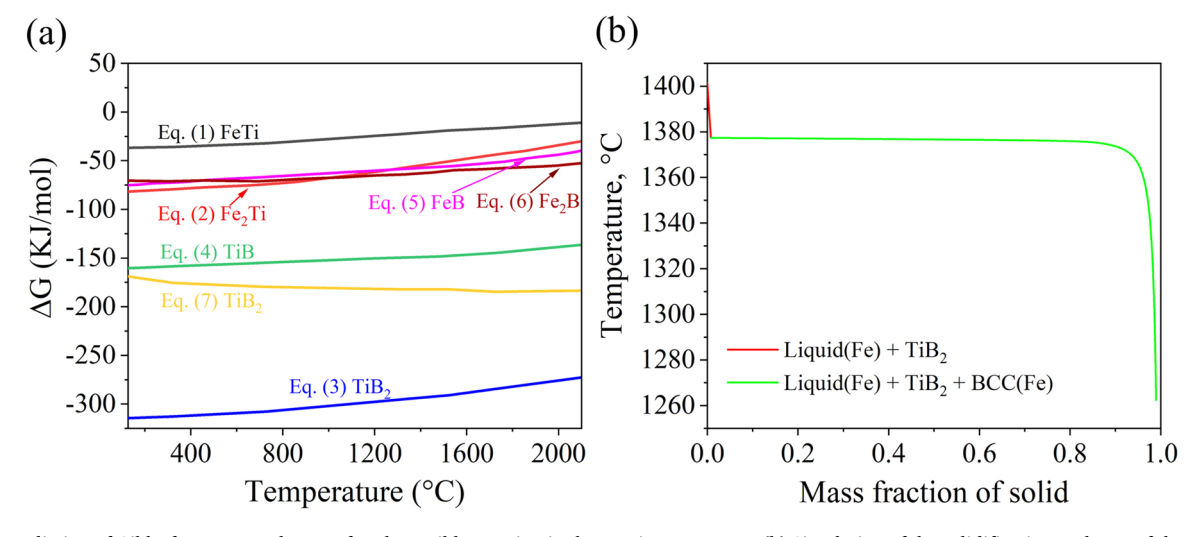


Fig. 7. (a) Prediction of Gibbs free-energy change of each possible reaction in the Fe-Ti-Fe₂B system. (b) Simulation of the solidification pathway of the Fe-Ti-B HMS based on Scheil-Gulliver non-equilibrium solidification model.

In order to analyze the competition among these reactions during LPBF, the changes in Gibbs free energy, ΔG , for these reactions were calculated, based on the thermodynamic data from Ref. [64] and are plotted in Fig. 7a. The calculated results demonstrate that all these reactions have a negative ΔG value, indicative of spontaneous reactions. Additionally, we observed that a more negative ΔG value was expected for reaction (3), i.e., $Ti + 2B = TiB_2$. Therefore, in our current system, reaction (3) is more energetically favored and is expected to prevail during the in-situ reaction, indicating that the TiB2 phase would form. Such analysis offers a theoretical background for our experimental results (Figs. 4, 5, and 6), namely, besides the α-Fe phase, only the TiB₂ phase was detected without any other reaction products. In order to get deeper physical insight into the formation mechanism of the TiB2 phase, Scheil-Gulliver solidification calculation was also performed. Fig. 7b presents the evolution of the phase fractions with respect to temperatures. Clearly, a solidification path: Liquid \rightarrow Liquid(Fe) + TiB₂ \rightarrow Liquid (Fe) + TiB₂ + BCC(Fe) is predicted. In other words, TiB₂ phase preferentially solidifies from the melt at the initial stage of rapid solidification.

3.2.2. Equiaxed grains with random crystallographic textures

In Section 3.2.1, a dual-phase structure containing both BCC-type α-Fe and HCP-type TiB₂ phases are revealed and discussed. In this section, we aim to understand the formation mechanism of equiaxed grains with random crystallographic textures. The EBSD results of the crosssections perpendicular to the building direction (top-view) and along the building direction (side-view) are respectively shown in the left and right columns of Fig. 8. It is clear from the inverse pole figure (IPF) maps that the α -Fe grains exhibit equiaxed morphologies in both top and side views (Fig. 8a and b). Also, relatively coarser grains are found in the HAZs below the melt pool boundaries (highlighted by the dash lines in Fig. 8b), which is in agreement with the SEM microstructural observation in Fig. 5. Fig. 8c and d display the α -Fe grain size distributions of the top- and side-view cross-sections of the LPBF HMS sample, respectively. In the two planes, comparable average grain sizes of 450--460~nm are identified. Interestingly, the majority of α -Fe grains (> 98%) are ultrafine with sub-micron ($< 1 \mu m$) grain sizes. Both SEM and EBSD results verify that the ultra-fine equiaxed grains are prevalent in the LPBF HMS. Fig. 8e and f show the Kernel average misorientation (KAM) maps of the top-view and side-view cross-sections, respectively. Higher KAM values are identified at grain boundaries, as compared with those in the grain interiors. In general, high KAM values suggest large local misorientations that are related to a significant accumulation of geometrically necessary dislocations (GNDs) [65]. In the current study, the large number of TiB2 nanoparticles at the grain boundaries understandably results in a larger lattice strain. As a result, a high density of GNDs is present at grain boundaries to accommodate the local strain incompatibility. Furthermore, no distinct KAM values were observed in the top-view and side-view cross-sections, suggesting an overall uniform microstructure (Fig. 8g and h).

In addition to the ultrafine equiaxed grains, we also note the random crystallographic textures, as indicated by the random grain colors in the EBSD IPF maps in Fig. 8a and b. To quantify the crystallographic texture, the pole figures of the α -Fe phase are extracted and are displayed in Fig. 9. Data is contoured by multiples of a uniform distribution (MUD), which is used as an indicator of the local texture intensity. MUD = 1 corresponds to a random distribution of crystal orientations. The pole figures in both top- and side-views (Fig. 9a and b) verify rather random crystallographic textures, with a maximum MUD of only 1.68 and 1.81, respectively. Such random crystallographic textures in our LPBF HMS are highly desirable for many structural applications. This observation stands in contrast to many other AM metal alloys, where the directional thermal gradients during LPBF often favor the epitaxial growth of columnar grains associated with strong crystallographic textures [56,57, 66]. Fig. 10a and b display the Taylor factor maps in both top- and side-views, where the lowest and highest values of M are shown in blue and red, respectively. The top- and side-views show similar average Taylor factor values of $\overline{M}\approx 3.05$ and 3.06, respectively (Fig. 10c and d), which indicate a nearly isotropic microstructure.

The formation of ultrafine equiaxed grains with random crystallographic textures are believed to be closely related to the TiB2 nanoparticles. As revealed in Section 3.2.1, the TiB₂ nanoparticles are preferentially formed at the initial stage of solidification. The TiB₂ phase was reported to have a favorable crystallographic-orientation relationship with the α -Fe phase, i.e., $[0001]_{TiB2}//[001]_{Fe}$ and $(10\overline{1}0)_{TiB2}//$ (100)_{Fe} [67,68]. The TEM characterization in Fig. 6 also confirms that the TiB₂ are either spherical or slightly faceted, which is suggestive of a semi-coherent interface between the TiB_2 nanoparticle and α -Fe matrix. In addition, Fig. S3 in the Supplementary Information shows the TEM images of the interface of the α-Fe and TiB₂ which is accompanied by lattice misfit dislocations, also indicative of semi-coherent interfaces. Such specific crystallographic orientations allow the in situ formed TiB₂ nanoparticles in the melt pool to serve as effective heterogeneous nucleation sites for the solidification of α -Fe phase, and consequently, promote the heterogenous nucleation of equiaxed crystals in the solidification front. Based on the classic solidification theory, the prevalence of equiaxed crystals in the solidification front would hinder the columnar grain growth, if any, and promote the columnar-to-equiaxed transition (CET). As such, the equiaxed grain morphology is formed. We also notice that the TiB₂ nanoparticles are preferentially distributed at the grain boundaries (Fig. 5c-d), which can inhibit the growth or coarsening of α -Fe grains due to the Zener pinning effect [69]. Furthermore, the random orientation of individual nanoscale TiB₂ nucleation agents in the melt pool determines the random orientation of newly formed equiaxed α -Fe grains, contributing to the development of random crystallographic textures. Collectively, ultrafine equiaxed grains with random crystallographic textures are formed in our LPBF Fe-TiB2 HMS.

3.3. Mechanical behavior

3.3.1. Mechanical properties

Fig. 11 exhibits the quasi-static compressive engineering stress-strain curves of our LPBF Fe-TiB2 HMS along both transverse and longitudinal directions. In the former case, the loading direction (LD) is perpendicular to the building direction (BD), while in the latter case, the LD is parallel to the BD. Table 1 summarizes the measured values of yield strength (σ_V) , fracture strength (σ_f) , fracture strain (ε_D) , and Young's modulus (E). Of particular interest, the LPBF Fe-TiB2 HMS exhibits exceptional and almost isotropic mechanical properties along the two different orientations with $E \approx 240$ GPa, $\sigma_y \approx 1450$ MPa, \approx 2000 MPa, and $\varepsilon_{\rm p}\approx$ 20%, giving rise to a high specific stiffness of $E/\rho\approx$ 34 GPa·cm³·g⁻¹ combined with a high specific yield strength of 207 MPa·cm³·g⁻¹ and a specific compressive strength of 272 MPa·cm³·g⁻¹. The mechanical properties are superior to those of some conventional HMSs such as press-hardened 22MnB5 steel, which often shows a specific stiffness of ~27 GPa·cm³·g⁻¹ and a specific yield strength of ~147 MPa·cm³·g⁻¹ [70,71]. Additionally, the average hardness of our LPBF Fe-TiB2 HMS in side- and top-views were measured to be 383.6 \pm 9.3 HV and 389 \pm 5.1 HV, respectively. It is worth mentioning that the isotropic mechanical properties of our LPBF HMS stand contrast to many other AM metal alloys with severe mechanical anisotropy [56,57,72,73]. The isotropic mechanical properties of the LPBF HMS are largely attributed to the random crystallographic textures.

3.3.2. Strengthening mechanisms

To probe into the fundamental strengthening mechanisms of our LPBF Fe-TiB₂ HMS, a quantitative estimate of the yield strength was performed. Owing to the isotropic microstructure and mechanical properties, here only the estimate of the yield strength along the

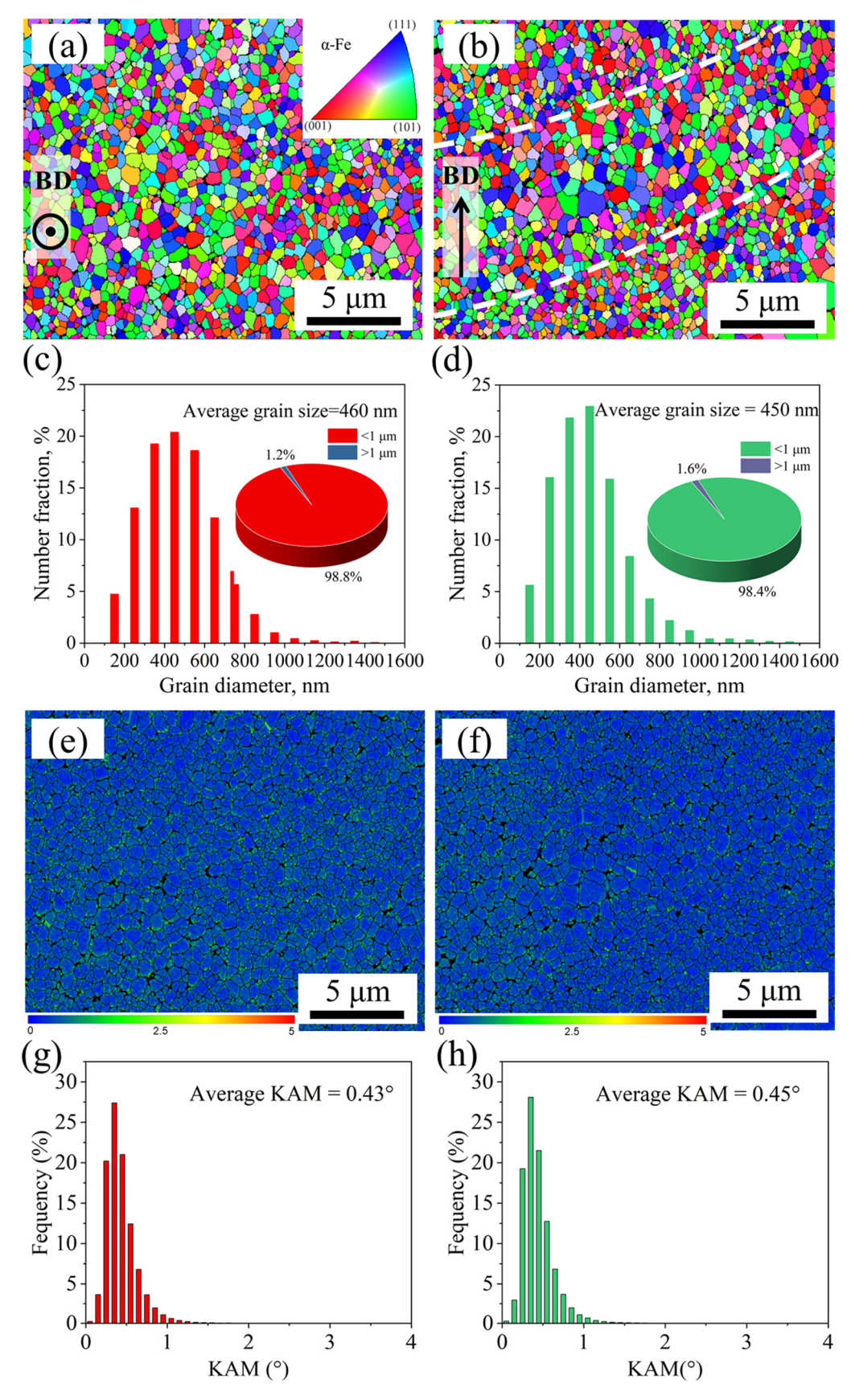


Fig. 8. EBSD characterization of LPBF HMS (a, b) IPF maps, (c, d) grain size distribution, (e, f) KAM maps, and (g, h) KAM distributions of (a, c, e, g) top- and (b, d, f, h) side-view cross-sections of the LPBF HMS. The building direction (BD) is shown with respect to the specimen coordinates. The KAM scale ranges from blue to red, representing 0–5° misorientation.

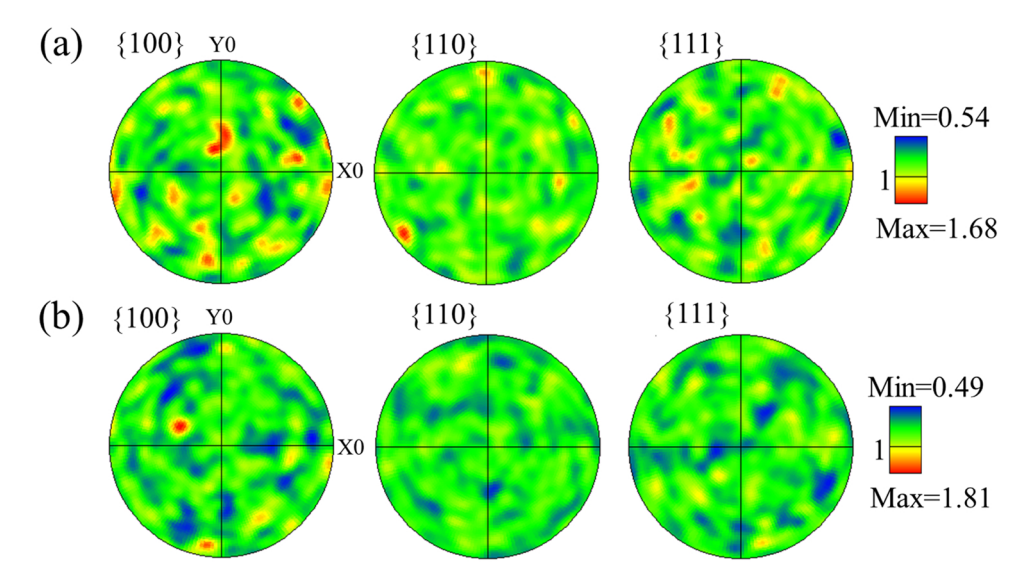


Fig. 9. Pole figures (PFs) of the LPBF HMS specimen. (a) top view. (b) side view.

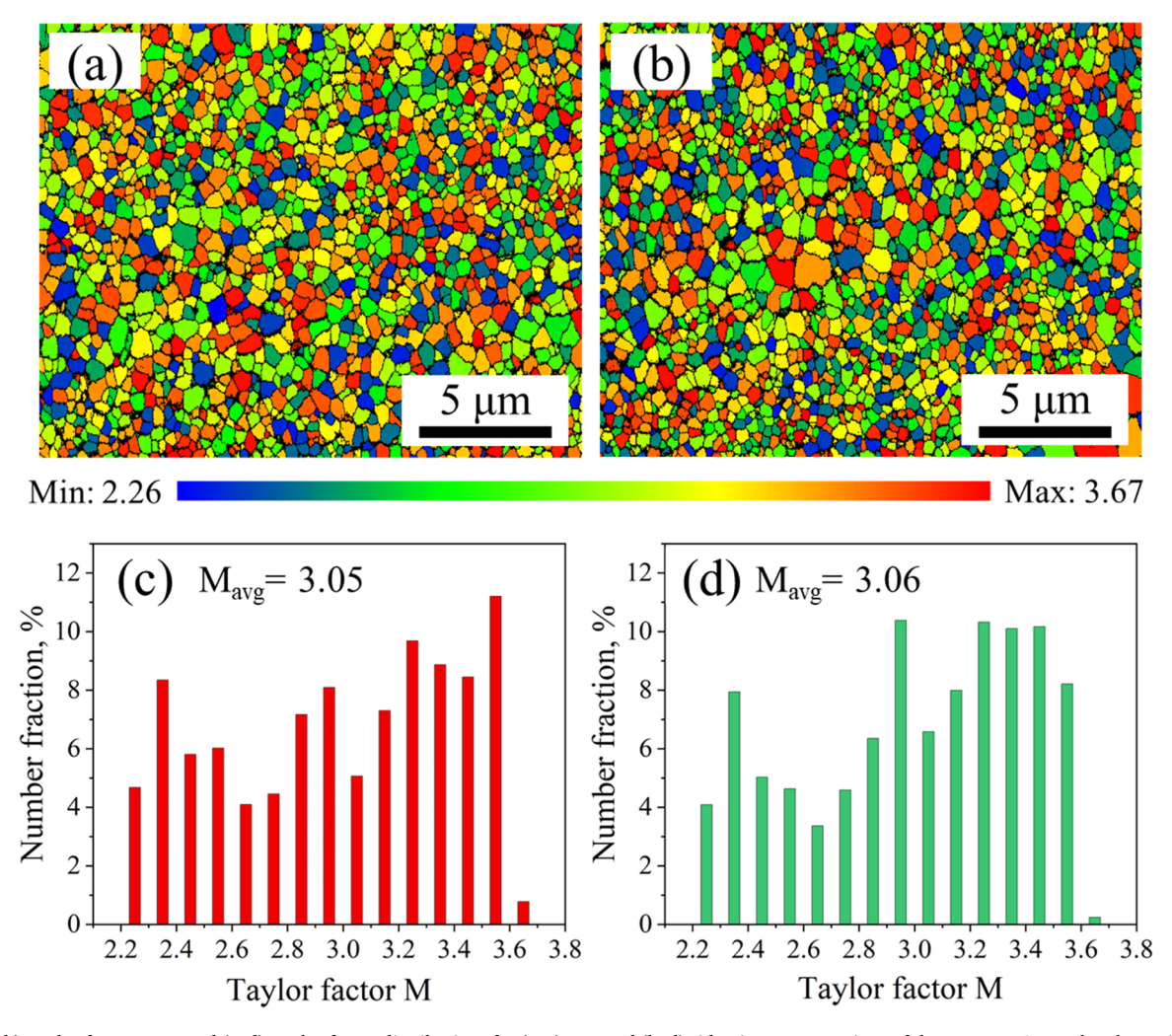


Fig. 10. (a, b) Taylor factor maps and (c, d) Taylor factor distributions for (a, c) top- and (b, d) side-view cross-sections of the LPBF HMS sample. The grains in the (a, b) Taylor factor maps are colorized to indicate the Taylor factor values.

transverse direction was conducted. The yield strength (σ_y) of LPBF HMS can be estimated by considering the frictional stress (σ_0) , dislocation strengthening $(\Delta\sigma_D)$, grain-boundary strengthening $(\Delta\sigma_G)$, and Orowan

strengthening (
$$\Delta\sigma_{\rm Orowan}$$
), as expressed by Eq. (9):
$$\sigma_{\rm y} = \sigma_0 + \Delta\sigma_{\rm D} + \Delta\sigma_{\rm G} + \Delta\sigma_{\rm Orowan} \eqno(9)$$

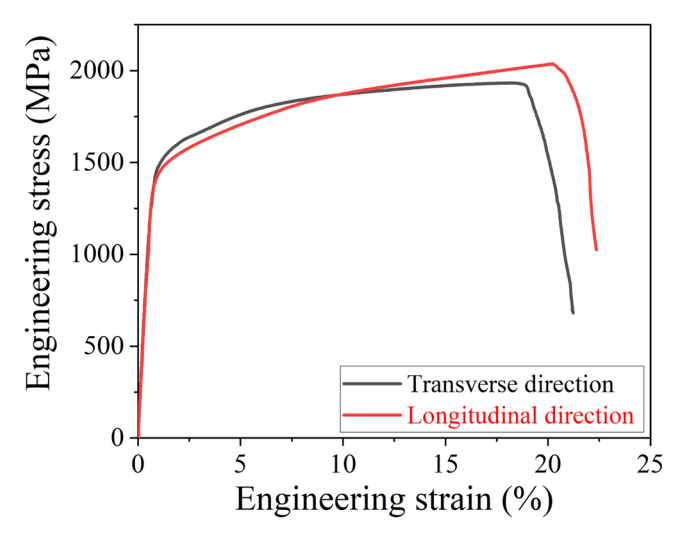


Fig. 11. Compressive engineering stress-strain curves of the LPBF HMS samples along transverse and longitudinal directions.

Table 1
Mechanical properties of the LPBF HMS sample along transverse and longitudinal directions.

Orientations	Young's modulus E (GPa)	Yield strength $\sigma_{ m y}$ (MPa)	Compressive strength $\sigma_{\rm f}$ (MPa)	Fracture strain $\varepsilon_{\rm p}$ (%)
Transverse Longitudinal	$\begin{array}{c} 241.6 \pm 3.8 \\ 238.3 \pm 4.5 \end{array}$	$1473\pm26\\1421\pm35$	$\begin{array}{c} 1937\pm39 \\ 2032\pm46 \end{array}$	$18.8 \pm 3.1 \\ 20.3 \pm 2.6$

where $\sigma_0 \approx 50$ MPa represents the frictional stress of the α -Fe steel matrix [74]. The LPBF HMS possesses a high density of dislocations, as indicated by EBSD KAM maps in Fig. 5e-f. The high dislocation density is believed to result from the large thermal residual stresses during LPBF, and these pre-existing dislocations would serve as obstacles for dislocation motion, inducing the so-called dislocation strengthening [75]. The dislocation strengthening can be calculated from the following Taylor hardening law [76]:

$$\Delta \sigma_{\rm D} = {\rm M}\alpha {\rm Gb} \rho^{1/2} \tag{10}$$

where α is the dimensionless pre-factor (\sim 0.24 for the BCC phase) [29], b=0.248 nm is the magnitude of the Burgers vector, M is the average Taylor factor, G=78 GPa is the shear modulus of the matrix [77], and ρ is the dislocation density. Here we use geometrically necessary dislocations (GNDs) to roughly represent the overall dislocation density and the GND density can be calculated based on the average KAM value, using the following formula [78]:

$$\rho = \frac{2\theta_{KAM}}{rh} \tag{11}$$

where $\theta_{\rm KAM}$ is the average KAM value (here, $\theta_{\rm KAM}\approx 0.0079$ for the sample in the transverse direction). x is the unit length, x=2 Px, where Px is the step size of the EBSD scan. Therefore, $\rho_{\rm GND}\approx 1.05\times 10^{15}$ m $^{-2}$, and thus, $\Delta\sigma_{\rm D}$ can be determined to be ~ 385 MPa. The grain-boundary strengthening can be calculated from the Hall-Petch relationship as follows [79]:

$$\Delta \sigma_G = K_{HP} d^{-1/2} \tag{12}$$

where $K_{HP}=17.4\,\mathrm{MPa~mm}^{1/2}$ represents the Hall-Petch coefficient [77], and d is the average grain size. Hence, the grain-boundary strengthening contribution is estimated to be 820 MPa. The Orowan mechanism operates if the nanoparticles inhibit dislocations, leads to

bowing dislocations around particles and creates strengthening effect. The contribution from the Orowan strengthening mechanism can be calculated as [80]:

$$\Delta \sigma_{or} = \frac{0.4M}{\pi \sqrt{1 - v}} \bullet \frac{Gb}{L} \bullet \ln \frac{\sqrt{\frac{2}{3}} d_p}{b}$$
 (13)

where

$$L = \sqrt{\frac{2}{3}} d_p \left(\sqrt{\frac{\pi}{4\nu_p} - 1} \right) \tag{14}$$

and M is again the Taylor factor of 3.05, ν denotes Poisson's ratio (0.29) of α -Fe [81], L is the interparticle spacing, b=0.248 nm is again the Burgers vector, d_p represents the mean particle diameter (\sim 98 nm), and ν_p is the volume fraction of the TiB₂ particles (13%). The calculated strength from the Orowan-strengthening mechanism in the sample is \sim 288 MPa.

Altogether, the total yield strength from various strengthening mechanisms is ~ 1543 MPa for the transverse direction. The calculated results agree reasonably well with the experimentally measured yield stress of 1473 MPa. The difference between the calculated and experimental values may be attributed to the overestimated Orowan-strengthening effect. In the present work, all the TiB2 nanoparticles ($\sim 13~\text{vol}\%$) were used for the theoretical calculation of the Orowan strengthening. However, according to the Orowan-strengthening mechanism, the interaction between the dislocations in the matrix and dispersed reinforcement particles contributes to the strengthening. The TiB2 particles located at the grain boundaries (Fig. 5c-d) may not provide an Orowan-strengthening effect, thus generating the overestimated strength.

3.3.3. Deformation micro-mechanisms

To reveal the deformation micro-mechanisms of our LPBF Fe-TiB2 HMS during compression, in situ synchrotron HE-XRD compression tests were performed. Fig. 12a shows the elastic lattice strain evolution versus applied stress in the loading direction for selected crystallographic planes of both α-Fe and TiB₂ phases. Three stages can be clearly identified from the curve of the elastic lattice strain vs. the applied stress. In stage I, a linear response of the elastic lattice strain to the applied stress was observed for all crystallographic planes of both phases, indicative of elastic deformation occurring in both phases. Different slopes of various crystallographic planes of both phases result from elastic anisotropy. Notably, the elastic diffraction constants of the TiB2 phase are significantly larger than those of the α -Fe phase, especially TiB₂ – {100}, {110}, and {111} grains. Hence, the incorporation of the TiB2 nanoparticles into the α-Fe matrix leads to a high Young's modulus. In stage II, the α -Fe crystallographic planes gradually yield, as evidenced from the decreased lattice strains. In this stage, the elastic lattice strains of TiB2 crystallographic planes also deviate from linearity but increase more rapidly. It is worth mentioning that in this stage, the TiB2 phase is still in the elastic region, and the sharp increases in the elastic lattice strains of the TiB2 crystallographic planes are due to the gradual load transfer from the $\alpha\textsc{-}\mbox{Fe}$ phase to the TiB_2 phase. After macroscopic yielding (stage III), the elastic lattice strains of various crystallographic planes of both phases increase simultaneously. Yet, the elastic lattice strains of TiB₂ crystallographic planes are much larger than those of α-Fe phase, manifesting that the TiB2 phase bears higher stresses than the α-Fe phase. To vividly demonstrate the real-time stress partition between the α -Fe and TiB₂ phases, the phase-specific stress, σ_{phase} , was estimated, using Hooke's law as follows:

$$\sigma_{phase} = \varepsilon_{phase} \bullet E_{phase} \tag{15}$$

where ε_{phase} is the phase-specific strain, and E_{phase} is the phase-specific Young's modulus. Here for the α -Fe phase, the {211} crystallographic

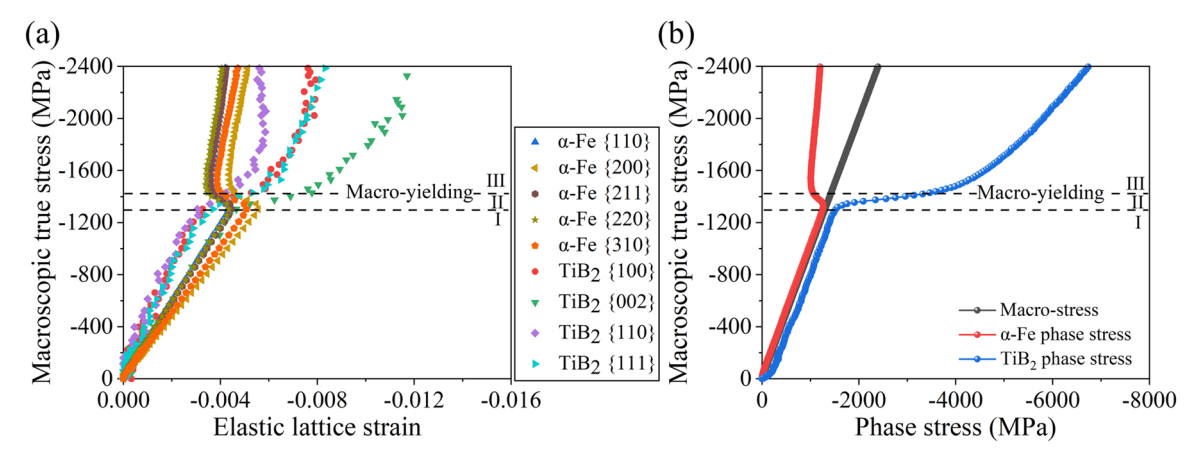


Fig. 12. (a) Elastic lattice-strain evolution of representative crystallographic planes along the loading direction of the α-Fe and TiB₂ phases during compression. (b) Stress-partition behavior between the α -Fe and TiB₂ phases during compression.

plane was selected to represent the average behavior of the α -Fe phase owing to its relatively low asymmetry and insensitivity to the intergranular strain [82]. The TiB₂ phase stress, σ_{TiB_2} , was then back calculated, based on the rule-of-mixture as follows:

$$\sigma_{TiB_2} = (\sigma_{applied} - \sigma_{\alpha - Fe} \bullet f_{\alpha - Fe}) / f_{TiB_2}$$
(16)

where $\sigma_{applied}$ is the applied macroscopic stress, and $f_{\alpha-Fe}$ and f_{TiB_2} are the volume fractions of the α-Fe and TiB2 phases, respectively. The phasespecific stresses of both $\alpha\text{-Fe}$ and TiB_2 structures as a function of the applied macroscopic true stress are plotted in Fig. 12(b). Clearly, in the elastic deformation region (region I), a slight stress partition is established between both phases. With further straining (regions II and III), increasingly higher stresses are transferred from the softer α -Fe matrix to the harder TiB2 nanoparticles, leading to significant increases of the macroscopic flow stress, i.e., strain hardening effect, and thus a large plasticity and a high fracture strength. The good damage tolerance of our LPBF Fe-TiB2 HMS can be attributed to the in-situ reaction-induced good interfacial cohesion and the spherical, nanoscale, and homogenously distributed TiB₂ particles. In contrast to the TiB₂ particles in the as-cast Fe-TiB2 HMS that are often deliberately added instead of by insitu chemical reaction, our in-situ synthesized Fe-TiB2 HMS by LPBF expectedly possess a stronger interfacial cohesion between the matrix and the reinforcing particles, which helps increase the plastic deformability around the interface and hence delay the interfacial de-bonding during loading [14]. Secondly, the ex-situ TiB₂ particles in the as-cast Fe-TiB₂ HMS are normally large and sharp-edged, and tend to cluster together, which could result in elevated stress concentration, damage percolation, and premature failure during loading [83,84]. In contrast, the TiB_2 particles in our LPBF Fe- TiB_2 HMS are spherical with an average size below 200 nm and are homogenously distributed, which help delocalize the strain during loading. As such, a good damage tolerance is expected for our LPBF Fe-TiB2 HMS.

4. Conclusions

In this study, Fe-TiB $_2$ HMS was fabricated by LPBF of mixed powders of Fe, Ti, and Fe $_2$ B, which are commercially available. Standard single-track experiments followed by printing and analysis of bulk samples enabled us to determine the optimal printing parameters for this mixed-powder system. The phase constitution, microstructure, and mechanical behavior of the LPBF Fe-TiB $_2$ composite HMS were studied and discussed. The important specific findings are summarized as follows:

(1) The LPBF Fe-TiB $_2$ nanocomposite HMS has a dual-phase structure containing a BCC α -Fe matrix and HCP TiB $_2$ nanoparticles, as evidenced by HE-XRD, SEM, and TEM analyses. The changes in

- Gibbs free energy, ΔG , for each possible reaction and Scheil-Gulliver solidification pathway prediction concurrently demonstrate that TiB₂ nanoparticles preferentially solidify from the melt at the initial stage of rapid solidification.
- (2) The LPBF Fe-TiB $_2$ HMS exhibits ultrafine equiaxed α -Fe grains with random crystallographic textures, as revealed by EBSD characterization. The formation of such an equiaxed grained microstructure is attributed to the in-situ formed TiB $_2$ nanoparticles which can serve as effective heterogenous nucleation sites for the α -Fe grains and promote the columnar-to-equiaxed transition.
- (3) The LPBF Fe-TiB $_2$ HMS exhibits excellent and isotropic mechanical properties with a high elastic modulus of ~ 240 GPa, an ultrahigh yield strength of ~ 1450 MPa, and a large compressive plasticity of $\sim 20\%$. Quantitative analysis indicates that the ultrahigh yield strength mainly originates from strengthening contributions of ultrafine grains of ~ 450 nm, nanoscale TiB $_2$ particles of 20–180 nm, and a high density of printing-induced dislocations of the order of $10^{15}~{\rm m}^{-2}$. In situ synchrotron HE-XRD reveals that the stress transfer progressively occurs from the α -Fe matrix to the stiffer and stronger TiB $_2$ nanoparticles during loading, leading to significant increases in the macroscopic flow stresses, i.e., pronounced strain-hardening effect and thus high fracture strength.

CRediT authorship contribution statement

Beyer Kevin: Data curation. Li Tianyi: Data curation. Fan Xuesong: Data curation. Mooraj Shahryar: Data curation. Luebbe Matthew: Data curation. Gerasimidis Simos: Writing – review & editing, Supervision, Funding acquisition. Guan Shuai: Writing – review & editing, Writing – original draft, Supervision, Formal analysis. Chen Wen: Writing – review & editing, Writing – original draft, Supervision, Funding acquisition, Formal analysis, Conceptualization. Zhang Shengbiao: Data curation. liaw peter: Supervision. wen haiming: Supervision. Feng Shuai: Writing – review & editing, Writing – original draft, Data curation. liu jian: Data curation. kong jian: Supervision.

Declaration of Competing Interest

The authors declare that they have no known competing financial interests or personal relationships that could have appeared to influence the work reported in this paper.

Data Availability

Data will be made available on request.

Acknowledgements

W.C. greatly acknowledges support from the UMass Amherst Faculty Startup Fund and National Science Foundation (DMR-2004429). This research used resources of the Advanced Photon Source, a U.S. Department of Energy (DOE) Office of Science user facility operated for the DOE Office of Science by Argonne National Laboratory under Contract No. DE-AC02–06CH11357. S.G. acknowledges support from the National Science Foundation (Grant No. CAREER CMMI-2044705). P.K. L. is great for the supports from the National Science Foundation (DMR-1611180 and 1809640) with program directors, Drs. J. Madison, J. Yang, G. Shiflet, and D. Farkas. H.W. appreciates the support from the U. S. Nuclear Regulatory Commission Faculty Development Program (award number NRC 31310018M0044).

Appendix A. Supporting information

Supplementary data associated with this article can be found in the online version at doi:10.1016/j.addma.2023.103569.

References

- [1] R. Rana, High modulus steels, Can. Metall. Q. 53 (2014) 241–242, https://doi.org/ 10.1179/0008443314Z.000000000178.
- [2] F. Akhtar, Ceramic reinforced high modulus steel composites: processing, microstructure and properties, Can. Metall. Q. 53 (2014) 253–263, https://doi.org/ 10.1179/1879139514Y.0000000135.
- [3] F. Bonnet, V. Daeschler, G. Petitgand, High modulus steels: new requirement of automotive market. How to take up challenge? Can. Metall. Q 53 (2014) 243–252, https://doi.org/10.1179/1879139514Y.0000000144.
- [4] R. Rana, C. Liu, Effects of ceramic particles and composition on elastic modulus of low density steels for automotive applications, Can. Metall. Q. 53 (2014) 300–316, https://doi.org/10.1179/1879139514Y.0000000130.
- [5] K. Tanaka, T. Saito, Phase equilibria in TiB₂-reinforced high modulus steel, J. Phase Equilib. 20 (1999) 207–214, https://doi.org/10.1361/105497199770335730.
- [6] H. Springer, C. Baron, A. Szczepaniak, V. Uhlenwinkel, D. Raabe, Stiff, light, strong and ductile: nano-structured High Modulus Steel, Sci. Rep. 7 (2017) 2757, https:// doi.org/10.1038/s41598-017-02861-3.
- [7] C. Baron, H. Springer, D. Raabe, Efficient liquid metallurgy synthesis of Fe-TiB₂ high modulus steels via in-situ reduction of titanium oxides, Mater. Des. 97 (2016) 357–363. https://doi.org/10.1016/j.matdes.2016.02.076.
- [8] S. Chen, P. Seda, M. Krugla, A. Rijkenberg, High-modulus steels reinforced with ceramic particles through ingot casting process, Mater. Sci. Technol. 32 (2016) 992–1003, https://doi.org/10.1080/02670836.2015.1104082.
- [9] A. Antoni-Zdziobek, M. Gospodinova, F. Bonnet, F. Hodaj, Experimental determination of solid-liquid equilibria with reactive components: example of the Fe-Ti-B ternary system, J. Phase Equilib. Diffus. 35 (2014) 701–710, https://doi. org/10.1007/s11669-014-0355-1.
- [10] R.G. Munro, Material properties of titanium diboride, J. Res. Natl. Inst. Stand. Technol. 105 (2000) 709, https://doi.org/10.6028/jres.105.057.
- [11] A. Antoni-Zdziobek, M. Gospodinova, F. Bonnet, F. Hodaj, Solidification paths in the iron-rich part of the Fe-Ti-B ternary system, J. Alloy. Compd. 657 (2016) 302–312, https://doi.org/10.1016/j.jallcom.2015.10.104.
- [12] R. Aparicio-Fernández, H. Springer, A. Szczepaniak, H. Zhang, D. Raabe, In-situ metal matrix composite steels: Effect of alloying and annealing on morphology, structure and mechanical properties of TiB₂ particle containing high modulus steels, Acta Mater. 107 (2016) 38–48, https://doi.org/10.1016/j.actamat.2016.01.048.
- [13] L. Cha, S. Lartigue-Korinek, M. Walls, L. Mazerolles, Interface structure and chemistry in a novel steel-based composite Fe-TiB₂ obtained by eutectic solidification, Acta Mater. 60 (2012) 6382–6389, https://doi.org/10.1016/j. actamat.2012.08.017.
- [14] M.X. Huang, B.B. He, X. Wang, H.L. Yi, Interfacial plasticity of a TiB₂-reinforced steel matrix composite fabricated by eutectic solidification, Scr. Mater. 99 (2015) 13–16, https://doi.org/10.1016/j.scriptamat.2014.11.015.
- [15] S. Zheng, R. Rementeria, W. Kan, M. Xu, J. Huang, Y. Huang, X. Pan, D. Apelian, Y. Liang, J. Lin, M. Perez, X. Li, Nanoparticle enabled high performance high modulus steels, Scr. Mater. 201 (2021), 113954, https://doi.org/10.1016/j.scriptamat.2021.113954.
- [16] M. Ziemnicka-Sylwester, L. Gai, S. Miura, Effect of (Ti:B) atomic ratio on mechanical properties of TiB₂–Fe composites "in situ" fabricated via Selfpropagating High-temperature Synthesis, Mater. Des. 69 (2015) 1–11, https://doi. org/10.1016/j.matdes.2014.12.036.

- [17] Y.Z. Li, M.X. Huang, Revealing the interfacial plasticity and shear strength of a TiB₂-strengthened high-modulus low-density steel, J. Mech. Phys. Solids 121 (2018) 313–327, https://doi.org/10.1016/j.jmps.2018.08.010.
- [18] Y.Z. Li, Z.C. Luo, H.L. Yi, M.X. Huang, Damage mechanisms of a TiB₂-reinforced steel matrix composite for lightweight automotive application, Metall. Mater. Trans. E. 3 (2016) 203–208, https://doi.org/10.1007/s40553-016-0088-7.
- [19] Z. Hadjem-Hamouche, K. Derrien, E. Héripré, J.-P. Chevalier, In-situ experimental and numerical studies of the damage evolution and fracture in a Fe-TiB₂ composite, Mater. Sci. Eng. A. 724 (2018) 594–605, https://doi.org/10.1016/j. msea 2018 03 108
- [20] H. Springer, R. Aparicio Fernandez, M.J. Duarte, A. Kostka, D. Raabe, Microstructure refinement for high modulus in-situ metal matrix composite steels via controlled solidification of the system Fe–TiB₂, Acta Mater. 96 (2015) 47–56, https://doi.org/10.1016/j.actamat.2015.06.017.
- [21] S. Guan, J. Ren, S. Mooraj, Y. Liu, S. Feng, S. Zhang, J. Liu, X. Fan, P.K. Liaw, W. Chen, Additive manufacturing of high-entropy alloys: microstructural metastability and mechanical behavior, J. Phase Equilib. Diffus. 42 (2021) 748–771, https://doi.org/10.1007/s11669-021-00913-w.
- [22] Y. Lu, S. Su, S. Zhang, Y. Huang, Z. Qin, X. Lu, W. Chen, Controllable additive manufacturing of gradient bulk metallic glass composite with high strength and tensile ductility, Acta Mater. 206 (2021), 116632, https://doi.org/10.1016/j. actamat.2021.116632.
- [23] L. He, S. Wu, A. Dong, H. Tang, D. Du, G. Zhu, B. Sun, W. Yan, Selective laser melting of dense and crack-free AlCoCrFeNi_{2.1} eutectic high entropy alloy: synergizing strength and ductility, J. Mater. Sci. Technol. 117 (2022) 133–145, https://doi.org/10.1016/j.jmst.2021.11.049.
- [24] Y. Zhou, F. Ning, P. Zhang, A. Sharma, Geometrical, microstructural, and mechanical properties of curved-surface AlSi10Mg parts fabricated by powder bed fusion additive manufacturing, Mater. Des. 198 (2021), 109360, https://doi.org/ 10.1016/j.matdes.2020.109360.
- [25] T. Voisin, J.-B. Forien, A. Perron, S. Aubry, N. Bertin, A. Samanta, A. Baker, Y. M. Wang, New insights on cellular structures strengthening mechanisms and thermal stability of an austenitic stainless steel fabricated by laser powder-bedfusion, Acta Mater. 203 (2021), 116476, https://doi.org/10.1016/j.actamat.2020.11.018
- [26] T. Voisin, R. Shi, Y. Zhu, Z. Qi, M. Wu, S. Sen-Britain, Y. Zhang, S.R. Qiu, Y. M. Wang, S. Thomas, B.C. Wood, Pitting corrosion in 316L stainless steel fabricated by laser powder bed fusion additive manufacturing: a review and perspective, JOM 74 (2022) 1668–1689, https://doi.org/10.1007/s11837-022-05206-2.
- [27] F. Ning, Y. Hu, Z. Liu, X. Wang, Y. Li, W. Cong, Ultrasonic vibration-assisted laser engineered net shaping of inconel 718 parts: microstructural and mechanical characterization, J. Manuf. Sci. Eng. Trans. 140 (2018), 061012, https://doi.org/ 10.1115/1.4039441.
- [28] A.N.M. Tanvir, Md.R.U. Ahsan, G. Seo, B. Bates, C. Lee, P.K. Liaw, M. Noakes, A. Nycz, C. Ji, D.B. Kim, Phase stability and mechanical properties of wire + arc additively manufactured H13 tool steel at elevated temperatures, J. Mater. Sci. Technol. 67 (2021) 80–94, https://doi.org/10.1016/j.jmst.2020.04.085.
- [29] J. Ren, Y. Zhang, D. Zhao, Y. Chen, S. Guan, Y. Liu, L. Liu, S. Peng, F. Kong, J. D. Poplawsky, G. Gao, T. Voisin, K. An, Y.M. Wang, K.Y. Xie, T. Zhu, W. Chen, Strong yet ductile nanolamellar high-entropy alloys by additive manufacturing, Nature 608 (2022) 62–68, https://doi.org/10.1038/s41586-022-04914-8.
- [30] Y.M. Wang, T. Voisin, J.T. McKeown, J. Ye, N.P. Calta, Z. Li, Z. Zeng, Y. Zhang, W. Chen, T.T. Roehling, R.T. Ott, M.K. Santala, P.J. Depond, M.J. Matthews, A. V. Hamza, T. Zhu, Additively manufactured hierarchical stainless steels with high strength and ductility, Nat. Mater. 17 (2018) 63–71, https://doi.org/10.1038/nmat5021.
- [31] H. Springer, C. Baron, F. Mostaghimi, J. Poveleit, L. M\u00e4dler, V. Uhlenwinkel, Additive manufacturing of high modulus steels: new possibilities for lightweight design, Addit. Manuf. 32 (2020), 101033, https://doi.org/10.1016/j. addma 2019.101033
- [32] B. AlMangour, D. Grzesiak, J.-M. Yang, Rapid fabrication of bulk-form TiB₂/316L stainless steel nanocomposites with novel reinforcement architecture and improved performance by selective laser melting, J. Alloy. Compd. 680 (2016) 489, 402, https://doi.org/10.1016/j.jiclleam.2016.04.156
- 480–493, https://doi.org/10.1016/j.jallcom.2016.04.156.
 [33] Y.K. Xiao, Z.Y. Bian, Y. Wu, G. Ji, Y.Q. Li, M.J. Li, Q. Lian, Z. Chen, A. Addad, H. W. Wang, Effect of nano-TiB₂ particles on the anisotropy in an AlSi10Mg alloy processed by selective laser melting, J. Alloy. Compd. 798 (2019) 644–655, https://doi.org/10.1016/j.jallcom.2019.05.279.
- [34] U. Essien, S. Vaudreuil, Issues in metal matrix composites fabricated by laser powder bed fusion technique: a review, Adv. Eng. Mater. 24 (2022) 2200055, https://doi.org/10.1002/adem.202200055.
- [35] U.A. Essien, S. Vaudreuil, In-situ metal matrix composites development for additive manufacturing: a perspective, J. Achiev. Mater. Manuf. Eng. 111 (2022) 78–85, https://doi.org/10.5604/01.3001.0015.9997.
- [36] S. Tjong, Microstructural and mechanical characteristics of in situ metal matrix composites, Mater. Sci. Eng. R. Rep. 29 (2000) 49–113, https://doi.org/10.1016/ S0927-796X(00)00024-3.
- [37] E.B. Baker, S. Jeon, O. Shuleshova, I. Kaban, Y. Wang, J. Gao, M. Kolbe, M. P. SanSoucie, D.M. Matson, Dendrite remelting during rapid solidification of undercooled CoSi-CoSi₂ eutectic alloys quantified by in situ synchrotron X-ray diffraction, Scr. Mater. 194 (2021), 113645, https://doi.org/10.1016/j.scriptamat.2020.113645.
- [38] S. Mooraj, J. Dong, K.Y. Xie, W. Chen, Formation of printing defects and their effects on mechanical properties of additively manufactured metal alloys, J. Appl. Phys. 132 (2022), 225108, https://doi.org/10.1063/5.0132137.

- [39] Y. Liu, J. Ren, S. Guan, C. Li, Y. Zhang, S. Muskeri, Z. Liu, D. Yu, Y. Chen, K. An, Y. Cao, W. Liu, Y. Zhu, W. Chen, S. Mukherjee, T. Zhu, W. Chen, Microstructure and mechanical behavior of additively manufactured CoCrFeMnNi high-entropy alloys: laser directed energy deposition versus powder bed fusion, Acta Mater. 250 (2023), 118884, https://doi.org/10.1016/j.actamat.2023.118884.
- [40] J. Ren, C. Mahajan, L. Liu, D. Follette, W. Chen, S. Mukherjee, Corrosion Behavior of Selectively Laser Melted CoCrFeMnNi High Entropy Alloy, Metals 9 (2019) 1029, https://doi.org/10.3390/met9101029.
- [41] N. Nadammal, T. Mishurova, T. Fritsch, I. Serrano-Munoz, A. Kromm, C. Haberland, P.D. Portella, G. Bruno, Critical role of scan strategies on the development of microstructure, texture, and residual stresses during laser powder bed fusion additive manufacturing, Addit. Manuf. 38 (2021), 101792, https://doi. org/10.1016/j.addma.2020.101792.
- [42] C.A. Schneider, W.S. Rasband, K.W. Eliceiri, NIH Image to ImageJ: 25 years of image analysis, Nat. Meth. 9 (2012) 671–675, https://doi.org/10.1038/ nmeth 2089
- [43] J. Schindelin, I. Arganda-Carreras, E. Frise, V. Kaynig, M. Longair, T. Pietzsch, S. Preibisch, C. Rueden, S. Saalfeld, B. Schmid, J.-Y. Tinevez, D.J. White, V. Hartenstein, K. Eliceiri, P. Tomancak, A. Cardona, Fiji: an open-source platform for biological-image analysis, Nat. Meth. 9 (2012) 676–682, https://doi.org/ 10.1038/nmeth.2019.
- [44] B.H. Toby, R.B.Von Dreele, GSAS-II: the genesis of a modern open-source all purpose crystallography software package, J. Appl. Crystallogr 46 (2013) 544–549, https://doi.org/10.1107/S0021889813003531.
- [45] K. Darvish, Z.W. Chen, T. Pasang, Reducing lack of fusion during selective laser melting of CoCrMo alloy: effect of laser power on geometrical features of tracks, Mater. Des. 112 (2016) 357–366, https://doi.org/10.1016/j.matdes.2016.09.086
- [46] L. Johnson, M. Mahmoudi, B. Zhang, R. Seede, X. Huang, J.T. Maier, H.J. Maier, I. Karaman, A. Elwany, R. Arróyave, Assessing printability maps in additive manufacturing of metal alloys, Acta Mater. 176 (2019) 199–210, https://doi.org/10.1016/j.actamat.2019.07.005.
- [47] W. Wang, J. Ning, S.Y. Liang, Analytical prediction of balling, lack-of-fusion and keyholing thresholds in powder bed fusion, Appl. Sci. 11 (2021) 12053, https:// doi.org/10.3390/app112412053.
- [48] L. Wang, Y. Zhang, H.Y. Chia, W. Yan, Mechanism of keyhole pore formation in metal additive manufacturing, Npj Comput. Mater. 8 (2022) 22, https://doi.org/ 10.1038/s41524-022-00699-6.
- [49] T. DebRoy, H.L. Wei, J.S. Zuback, T. Mukherjee, J.W. Elmer, J.O. Milewski, A. M. Beese, A. Wilson-Heid, A. De, W. Zhang, Additive manufacturing of metallic components process, structure and properties, Prog. Mater. Sci. 92 (2018) 112–224, https://doi.org/10.1016/j.pmatsci.2017.10.001.
- [50] E.O. Olakanmi, Selective laser sintering/melting (SLS/SLM) of pure Al, Al-Mg, and Al-Si powders: effect of processing conditions and powder properties, J. Mater. Process. Technol. 213 (2013) 1387–1405, https://doi.org/10.1016/j. imatprotec.2013.03.009.
- [51] Y.-H. Siao, C.-D. Wen, Examination of molten pool with Marangoni flow and evaporation effect by simulation and experiment in selective laser melting, Int. Commun. Heat. Mass Transf. 125 (2021), 105325, https://doi.org/10.1016/j. icheatmasstransfer.2021.105325.
- [52] A. Anal, T.K. Bandyopadhyay, K. Das, Synthesis and characterization of TiB2reinforced iron-based composites, J. Mater. Process. Technol. 172 (2006) 70–76, https://doi.org/10.1016/j.jmatprotec.2005.09.011.
- [53] C. Tian, X. Li, H. Li, G. Guo, L. Wang, Y. Rong, The effect of porosity on the mechanical property of metal-bonded diamond grinding wheel fabricated by selective laser melting (SLM), Mater. Sci. Eng. A. 743 (2019) 697–706, https://doi. org/10.1016/j.msea.2018.11.138.
- [54] Y. Yuan, W. Zhang, P. Zhang, X. Fan, M. Zhu, Porous grinding wheels toward alleviating the pre-fatigue and increasing the material removal efficiency for rail grinding, Tribol. Int. 154 (2021), 106692, https://doi.org/10.1016/j. triboint 2020 106692.
- [55] S. Li, B. Zhang, Q. Jiang, H. Han, J. Wen, C. Zhou, Formation characteristics of nickel-based diamond abrasive segment by selective laser melting, Opt. Laser Technol. 148 (2022), 107665, https://doi.org/10.1016/j.optlastec.2021.107665.
- [56] L. Thijs, M.L. Montero Sistiaga, R. Wauthle, Q. Xie, J.-P. Kruth, J. Van Humbeeck, Strong morphological and crystallographic texture and resulting yield strength anisotropy in selective laser melted tantalum, Acta Mater. 61 (2013) 4657–4668, https://doi.org/10.1016/j.actamat.2013.04.036.
- [57] A. Keshavarzkermani, M. Sadowski, L. Ladani, Direct metal laser melting of Inconel 718: process impact on grain formation and orientation, J. Alloy. Compd. 736 (2018) 297–305, https://doi.org/10.1016/j.jallcom.2017.11.130.
- [58] P. Hou, S. Mooraj, V.K. Champagne, M.J. Siopis, P.K. Liaw, S. Gerasimidis, W. Chen, Effect of build height on temperature evolution and thermally induced residual stresses in plasma arc additively manufactured stainless steel, Metall. Mater. Trans. A. 53 (2022) 627–639, https://doi.org/10.1007/s11661-021-06538-5
- [59] G. Wang, Y. Li, Y. Gao, L. Niu, Thermodynamic study on self-propagating high temperature synthesis of TiB₂/Fe composites, J. Wuhan. Univ. Technol. -Mat. Sci. Ed. 34 (2019) 769–773, https://doi.org/10.1007/s11595-019-2115-x.
- [60] C.C. Degnan, P.H. Shipway, The incorporation of self-propagating, high-temperature synthesis-formed Fe-TiB₂ into ferrous melts, Metall. Mater. Trans. A. 33 (2002) 2973–2983, https://doi.org/10.1007/s11661-002-0282-3.
- [61] A. Agarwal, N.B. Dahotre, Pulse electrode deposition of superhard boride coatings on ferrous alloy, Surf. Coat. Technol. 106 (1998) 242–250, https://doi.org/ 10.1016/S0257-8972(98)00545-3.

- [62] Y. Liu, B. Li, J. Li, L. He, S. Gao, T.G. Nieh, Effect of titanium on the ductilization of Fe–B alloys with high boron content, Mater. Lett. 64 (2010) 1299–1301, https://doi.org/10.1016/j.matlet.2010.03.013.
- [63] M.-H. Zhuang, M.-Q. Li, J. Wang, Z. Ma, Z.-Y. Zhou, Effect of Ti addition on phase constitution and wear resistance of Fe-B-C hypereutectic overlays produced using powder-wire composite arc welding, Mater. Trans. 58 (2017) 945–950, https://doi.org/10.2320/matertrans.M2016392.
- [64] D. Ye, J. Hu. The Thermodynamic Data of Inorganic Materials Handbook, Second ed., Metallurgical Industry Press, Beijing, 2002.
- [65] L.P. Kubin, A. Mortensen, Geometrically necessary dislocations and strain-gradient plasticity: a few critical issues, Scr. Mater. 48 (2003) 119–125, https://doi.org/ 10.1016/S1359-6462(02)00335-4.
- [66] L. Thijs, K. Kempen, J.-P. Kruth, J. Van Humbeeck, Fine-structured aluminium products with controllable texture by selective laser melting of pre-alloyed AlSi10Mg powder, Acta Mater. 61 (2013) 1809–1819, https://doi.org/10.1016/j. actamat.2012.11.052.
- [67] S. Lartigue-Korinek, M. Walls, N. Haneche, L. Cha, L. Mazerolles, F. Bonnet, Interfaces and defects in a successfully hot-rolled steel-based composite Fe–TiB₂, Acta Mater. 98 (2015) 297–305, https://doi.org/10.1016/j.actamat.2015.07.024
- [68] Y.F. Li, B. Xiao, G.L. Wang, L. Sun, Q.L. Zheng, Z.W. Liu, Y.M. Gao, Revealing the novel fracture mechanism of the interfaces of TiB₂/Fe composite from a first principles investigation, Acta Mater. 156 (2018) 228–244, https://doi.org/ 10.1016/j.actamat.2018.06.040.
- [69] B. Li, B. Qian, Y. Xu, Z. Liu, F. Xuan, Fine-structured CoCrFeNiMn high-entropy alloy matrix composite with 12 wt% TiN particle reinforcements via selective laser melting assisted additive manufacturing, Mater. Lett. 252 (2019) 88–91, https://doi.org/10.1016/j.matlet.2019.05.108.
- [70] B.-A. Behrens, S. Jüttner, K. Brunotte, F. Özkaya, M. Wohner, E. Stockburger, Extension of the conventional press hardening process by local material influence to improve joining ability, Procedia Manuf. 47 (2020) 1345–1352, https://doi.org/ 10.1016/j.promfg.2020.04.258.
- [71] S. Li, P. Wen, S. Li, W. Song, Y. Wang, H. Luo, A novel medium-Mn steel with superior mechanical properties and marginal oxidization after press hardening, Acta Mater. 205 (2021), 116567, https://doi.org/10.1016/j. actamat 2020 116567
- [72] T. Niendorf, S. Leuders, A. Riemer, H.A. Richard, T. Tröster, D. Schwarze, Highly anisotropic steel processed by selective laser melting, Metall. Mater. Trans. B. 44 (2013) 794–796, https://doi.org/10.1007/s11663-013-9875-z.
- [73] D. Ma, A.D. Stoica, Z. Wang, A.M. Beese, Crystallographic texture in an additively manufactured nickel-base superalloy, Mater. Sci. Eng. A. 684 (2017) 47–53, https://doi.org/10.1016/j.msea.2016.12.028.
- [74] F. Jiang, S. Takaki, T. Masumura, R. Uemori, H. Zhang, T. Tsuchiyama, Nonadditive strengthening functions for cold-worked cubic metals: experiments and constitutive modeling, Int. J. Plast. 129 (2020), 102700, https://doi.org/ 10.1016/i.iiplas.2020.102700.
- [75] K.M. Bertsch, G. Meric de Bellefon, B. Kuehl, D.J. Thoma, Origin of dislocation structures in an additively manufactured austenitic stainless steel 316L, Acta Mater. 199 (2020) 19–33, https://doi.org/10.1016/j.actamat.2020.07.063.
- [76] H. Chen, T. Lu, Y. Wang, Y. Liu, T. Shi, K.G. Prashanth, K. Kosiba, Laser additive manufacturing of nano-TiC particles reinforced CoCrFeMnNi high-entropy alloy matrix composites with high strength and ductility, Mater. Sci. Eng. A. 833 (2022), 142512, https://doi.org/10.1016/j.msea.2021.142512.
 [77] B. Song, S. Dong, S. Deng, H. Liao, C. Coddet, Microstructure and tensile properties
- [77] B. Song, S. Dong, S. Deng, H. Liao, C. Coddet, Microstructure and tensile properties of iron parts fabricated by selective laser melting, Opt. Laser Technol. 56 (2014) 451–460, https://doi.org/10.1016/j.optlastec.2013.09.017.
- [78] S. Peng, S. Mooraj, R. Feng, L. Liu, J. Ren, Y. Liu, F. Kong, Z. Xiao, C. Zhu, P. K. Liaw, W. Chen, Additive manufacturing of three-dimensional (3D)-architected CoCrFeNiMn high- entropy alloy with great energy absorption, Scr. Mater. 190 (2021) 46–51, https://doi.org/10.1016/j.scriptamat.2020.08.028.
- [79] Y. Wang, Z. Liu, Y. Zhou, X. Yang, J. Tang, X. Liu, J. Li, G. Le, Microstructure and mechanical properties of TiN particles strengthened 316L steel prepared by laser melting deposition process, Mater. Sci. Eng. A. 814 (2021), 141220, https://doi. org/10.1016/j.msea.2021.141220.
- [80] A. Sanaty-Zadeh, Comparison between current models for the strength of particulate-reinforced metal matrix nanocomposites with emphasis on consideration of Hall-Petch effect, Mater. Sci. Eng. A. 531 (2012) 112–118, https://doi.org/10.1016/j.msea.2011.10.043.
- [81] M. Tikhonchev, V. Svetukhin, Primary radiation damage of BCC iron under uniaxial and hydrostatic stress: MD simulation, Appl. Mech. Mater. 835 (2016) 197–202, https://doi.org/10.4028/www.scientific.net/AMM.835.197.
- [82] L. Ma, L. Wang, Z. Nie, F. Wang, Y. Xue, J. Zhou, T. Cao, Y. Wang, Y. Ren, Reversible deformation-induced martensitic transformation in Al_{0.6}CoCrFeNi highentropy alloy investigated by in situ synchrotron-based high-energy X-ray diffraction, Acta Mater. 128 (2017) 12–21, https://doi.org/10.1016/j. actamat.2017.02.014.
- [83] D. Wang, P. Shanthraj, H. Springer, D. Raabe, Particle-induced damage in Fe-TiB₂ high stiffness metal matrix composite steels, Mater. Des. 160 (2018) 557–571, https://doi.org/10.1016/j.matdes.2018.09.033.
- [84] H. Zhang, H. Springer, R. Aparicio-Fernández, D. Raabe, Improving the mechanical properties of Fe-TiB₂ high modulus steels through controlled solidification processes, Acta Mater. 118 (2016) 187–195, https://doi.org/10.1016/j. actamat.2016.07.056.